ACS OMEGA

Open Access

http://pubs.acs.org/journal/acsodf

Article

Structure and Dynamics of Confined Water Inside Diphenylalanine Peptide Nanotubes

Jinfeng Chen, Zongyang Qiu, and Jing Huang*

Cite This: *ACS Omega* 2023, 8, 42936−42950

Read Online

ACCESS | Metrics & More | Article Recommendations | Supporting Information

ABSTRACT: Diphenylalanine (FF) peptides exhibit a unique ability to self-assemble into nanotubes with confined water molecules playing pivotal roles in their structure and function. This study investigates the structure and dynamics of diphenylalanine peptide nanotubes (FFPNTs) using all-atom molecular dynamics (MD) and grand canonical Monte Carlo combined with MD (GCMC/MD) simulations with both the CHARMM additive and Drude polarizable force fields. The occupancy and dynamics of confined water molecules were also examined. It was found that less than 2 confined water molecules per FF help stabilize the FFPNTs on the $x-y$ plane. Analyses of the kinetics of confined water molecules revealed distinctive transport behaviors for bound and free water, and their respective diffusion coefficients were compared. Our results validate the importance of polarizable force field models in studying peptide nanotubes and provide insights into our understanding of nanoconfined water.

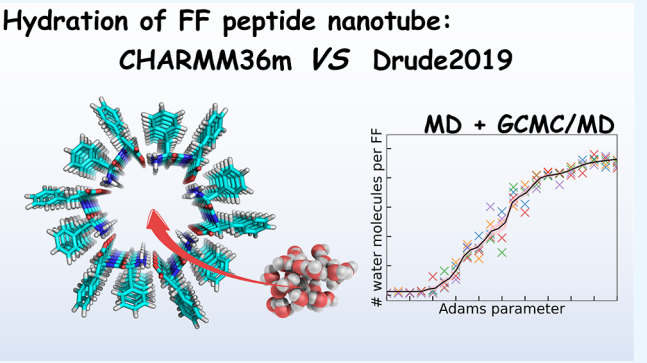

1. INTRODUCTION

Diphenylalanine peptides self-assemble into peptide nanotubes (PNT) with hydrophilic channels of approximately 10 Å in diameter, which was first observed and simultaneously characterized by X-ray crystallography in 2001.[1] The channel is formed by the head-to-tail combination of peptide terminals through the hydrogen bond donor and acceptor pair ($-NH_3^+$ and $-COO^-$). The peptide bonds with potential hydrophilic charged C and N termini are buried toward the channel pore, while those hydrophobic phenyl groups are exposed outside the channel. FFPNTs exhibit remarkable mechanical and electric properties, such as stronger-than-average point stiffness among PNTs[2] and robust piezoelectricity,[3] making them high-potential materials. FFPNTs and their derivatives have also been reported to be highly sensitive biosensors for detecting small molecules.[4,5]

From a biological point of view, FFPNTs can serve as a model system to mimic the functions of transmembrane channel proteins as they feature a hydrophilic pore lined with hydrophobic phenyl groups.[6,7] Furthermore, the assembly ability of short peptides containing phenylalanine or diphenylalanine was related to the formation of amyloid fibrils which is crucial in many diseases.[8−10] Diphenylalanine as the 19th and 20th residues in the Aβ peptides was shown to play a key role in their unfolding and aggregation.[11,12] Therefore, further applications of FFPNTs are limited by the challenges in understanding their potential cytotoxicity and compatibility with biosystems.[13,14] In the crystal structure, 9 water sites were resolved as shown in Figure 1a. These water sites differ in the occupancies and a total of 2.473 water molecules per FF were observed.[1] Confined water molecules are crucial for FFPNTs' desirable properties[2,15−17] and have a substantial effect on their self-assembly processes.[18] The abundance of $-COO^-$ and $-NH_3^+$ pairs in the interior wall of FFPNTs can slow down or even halt the self-assembly processes without water involvement, due to the difficulties in the formation of analogous buried salt bridges.[19] Water molecules cannot be ignored in molecular modeling and simulations of FFPNTs. For example, a first-principle calculation of FFPNT rigidity[20] with a high level of theory[21,22] yielded a Young modulus of ∼8.8 GPa, significantly lower than the ∼19−27 GPa measured by atomic force microscopy.[2,23] The reason was attributed to the neglect of water molecules in the calculations and the importance of water to FFPNT rigidity is further revealed by analyzing the lattice vibrations combined with Raman spectra by Zelenovskiy et al.[24] Similarly, ignoring the important role played by water molecules during MD simulations led to an overestimation of the contributions by the hydrophobic phenyl rings to the formation of hollow tubular structures.[25] Hence, a comprehensive understanding of FFPNTs necessitates realistic

Received: August 16, 2023
Revised: September 22, 2023
Accepted: October 19, 2023
Published: October 31, 2023

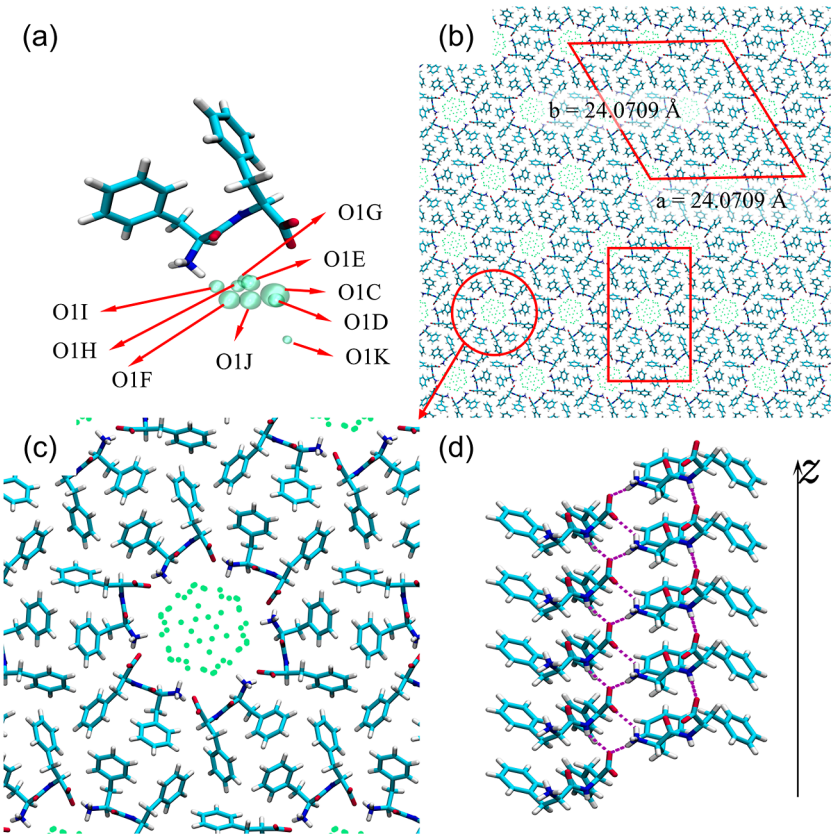

Figure 1. (a) Experimentally determined structure of a single L, L-FF molecule, along with the locations of 9 crystal water sites based on CCDC data. The size of each water site is plotted according to its occupancy measured by X-ray. (b) Projection of the FFPNTs on the $x-y$ plane. The red circle illustrates the channel formed by FFs, the red rhomboid contains the basic unit box for MD simulations, and the red rectangle contains the basic unit box for GCMC/MD simulations. (c) Channel formed by six FFs in a head-to-tail manner and the distribution of water sites in the channel. (d) Hydrogen bond networks formed between FFs with hydrogen bonds colored purple. Elements H, C, N, and O are colored white, cyan, blue, and red, respectively. Water sites are marked green.

modeling of the interactions between FFPNTs and their confined water along with careful investigations of their structural and dynamic properties.

Confined water molecules can form multilayers in the large channel of an FFPNT and fall into two types: bound water and free water. Water molecules directly interacting with the hydrophilic interior wall are defined as bound water, while others that are close to the channel center and interact with the bound water are classified as free water.[26] The distribution of these two types of confined water highly depends on the hydration state or relative humidity under experimental conditions. While 9 water sites have been resolved experimentally,[1] some of them are too close to each other (e.g., the water sites O1E and O1G are only 0.78 Å apart) such that they cannot be occupied simultaneously. Consideration of the hydration states is thus crucial for a reliable understanding of the distribution of these confined water molecules and their contributions to the FFPNTs' rigidity as well as their diffusion behaviors. A variety of methods have been developed to determine the hydration state in a chemical or biological system,[27−29] with physics-based simulation methods perhaps being the most reliable. In particular, sampling the system under the grand canonical (GC) ensemble is widely adopted for determining the number of small molecules inside a specific region[30,31] and exploring their binding modes, for example, studying the properties of water confined in carbon nanotubes (CNTs) .[32−36] We note that the use of grand canonical ensemble methods may suffer from the lack of proper excess chemical potential a priori, which is necessary to yield a desirable hydration state. To address this issue, several algorithms have been proposed.[37]

Apart from the spatial distribution of confined water inside nanotubes, the transport properties of these water molecules are another intriguing aspect that needs to be understood to make nanotubes powerful nanofluidic devices. The mean-square displacement (MSD) that describes the movement in specific time intervals has been widely adopted to describe the transport properties of confined water molecules. Theoretical and simulation investigations were particularly useful in these investigations.[38] In general, confined water molecules in nanotubes can exhibit three types of diffusion mechanisms: the classical Fickian mechanism in which the MSD scales linearly with time ($dr^2 \propto dt$); it often occurs in a large pore environment where water molecules can freely move along the pore direction; the single-file mechanism in which the MSD scales with the square root of time ($dr^2 \propto dt^{1/2}$) that is usually assumed to occur at very narrow pore size where water molecules can only move in one dimension and cannot pass each other; the ballistic mechanism in which the MSD scales with the square of time ($dr^2 \propto dt^2$) that is typically happened when water molecules move in a highly coordinated manner.[39] In most cases, the self-diffusion behavior of water molecules confined in nanotubes can be accurately described by Fick's law,[40] including the water transport in unmodified or modified

https://doi.org/10.1021/acsomega.3c06071
ACS Omega 2023, 8, 42936−42950

CNTs that have similar or slightly larger diameters than FFPNTs.[39] As measured by Zelenovskiy et al. through water vapor sorption, the self-diffusion of water confined in the FFPNTs exhibits the ballistic type when the number of water molecules is less than 0.83 per FF and the Fickian type when the number of water molecules increases.[26] However, bound water and free water cannot be distinguished with current state-of-the-art experimental methodologies, so their potentially different transport behaviors remain unclear. MD simulation constitutes an effective tool for understanding water dynamics in confined environments[38] as it can provide atomistic details on the motion of each water molecule.

To obtain meaningful insights into the structure and dynamic properties of confined water in FFPNTs, a proper computational level should be carefully chosen. Applying quantum chemistry (QM) based methods such as density functional tight binding (DFTB)[41,42] or ab initio level simulations provide accurate modeling of interactions but can suffer from the limitations of small system size and short time scale due to the high computational costs. For example, Andrade-Filho et al. performed DFTB-level MD simulations of a single unit cell of the FFPNTs with a time scale of 10 ps.[43] A similar system size was employed in the DFT calculations of FFPNTs by Bystrov et al.[44] In these works, the dynamics and kinetics of confined water molecules cannot be discussed, as with the use of periodic images the results tend to symmetrize the behavior of water molecules and introduce artifacts. The relatively short time scale may also lead to unreliable modeling of water transport, as it has been demonstrated that at least 500 ps simulations are needed to study water diffusion.[39] It was even argued that a time scale greater than 50 ns might be needed for the realistic modeling of water transport.[45]

In contrast, classical force fields offer the possibility to access meaningful time scales with realistic system sizes to simulate the FFPNT for investigating the roles and dynamics of confined water molecules. For CNTs, it is well known that modeling of the polarization effect and cation−π interactions would be important for the candidate force field models due to the conjugated π-electrons under nanoconfined conditions,[46,47] although additive fixed-charge force fields are still widely used.[48−50] In additive force fields, the polarization effects were implicitly included during the parametrization processes,[51,52] which are often sufficient to reproduce the ensemble average of general peptide and protein systems. How well additive force fields can be used to model peptide nanotubes such as FFPNT remains an open question, although capturing detailed polarization interactions might still be important for confined water molecules in peptide nanotubes.

The development of protein polarizable force fields has advanced significantly in the past decade,[53−56] in particular, the AMOEBA force field based on point-induced dipole[57,58] and the Drude force field based on classical Drude oscillator.[59−61] Polarizable force fields have been used to reveal the importance of polarization effects in modeling salt bridge interactions in proteins,[62] ion binding and selectivity,[63,64] helix formation,[65] amyloid aggregation,[66] and protein−ligand binding processes.[67−69] The recently developed Drude-2019 protein force field has further enhanced the accuracy of protein dynamics through adjustments of the polarizabilities of select C atoms, reoptimized of side chain χ_1, χ_2 dihedral parameters, and improved description of the interactions between charged residues.[60] To the best of our knowledge, the Drude polarizable force fields have not been applied to study peptide nanotube systems. While the FFPNT system involves only a single type of amino acid (Phe) and water, it could serve as a model system to test the transferability of the Drude polarizable force field.

In this work, we investigate the dynamic properties of water inside FFPNTs and evaluate the performance of the additive CHARMM and the polarizable Drude force fields. We carried out extensive MD simulations using these two force field models with different hydration states of the FFPNT. State-of-the-art grand canonical Monte Carlo (GCMC) simulations were combined with MD to study the distribution of water molecules inside the channel and the capability of FFPNTs to hold water. The transport behavior of bound water and free water was considered separately in a relatively large system at a time scale of 100 ns. These findings provide insights into the dynamics of confined water molecules and allow us to systematically examine the impact of polarization in the FFPNT system, which can be extended to other peptide nanotube systems and the behavior of nanoconfined water molecules.

2. METHODS

2.1. System Preparation. The L, L-FFPNT model was constructed using the $P6_1$ space group based on the X-ray crystal block structure downloaded from the Cambridge Crystallographic Data Center (CCDC) with the ID: 163340.[70] The simulation systems were built employing PyMOL[71] and CHARMM.[72] The additive CHARMM36m (C36m) force field[73] and the polarizable Drude-2019 force field[74] were used to model peptides. The TIP3P water model[75] modified for CHARMM force field that introduces van der Waals (vdW) parameters on the hydrogen atoms (also called mTIP3P)[52] and the SWM4-NDP model[76] were employed for simulations with C36m and Drude force fields, respectively.

2.2. MD Simulations. The FFPNTs were built to a supramolecular assembly containing 5 layers with 2 × 2 unit cells as shown by the red rhomboid in Figure 1. The crystal parameter becomes a = 48.141 Å, b = 48.141 Å, c = 27.280 Å, α = 90°, β = 90°, and γ = 120°, which results in a system with a total of 120 FFs. To understand the relationship between the number of water molecules and FFPNTs, our MD simulations considered 7 different initial hydration states including an empty FFPNTs system and 6 systems with different numbers of water molecules. These numbers of water molecules (N_w) correspond to 1, 2, 3, 4, 5, and 9 water molecules per FF, respectively, and will be referred to Sys_n in the following context where n is the corresponding number of water molecules per FF. The initial positions of these water molecules were randomly assigned to the experimentally resolved water sites.

In all MD simulations, periodic boundary conditions (PBC) were adopted and timesteps were set to 1 fs. Electrostatic interactions were treated with particle mesh Ewald summation with a real space cutoff of 12 Å.[77] VdW interactions were truncated at 12 Å with a switching function[78] applied between 10 and 12 Å. The SHAKE algorithm[79] was used to maintain the geometries of water molecules and the covalent bonds between heavy atoms and H atoms in MD simulations. No other constraints or restraints were applied. For all systems, the simulations were carried out at two temperatures: 150 and 298.15 K, which corresponded to the crystallography experiment temperature and room temperature, respectively. The crystal parameters have been reported to be insensitive to

https://doi.org/10.1021/acsomega.3c06071
ACS Omega 2023, 8, 42936−42950

temperature,[26] making the structure a reasonable initial model for both temperatures.

For the C36m force field, all systems were first heated to their corresponding temperatures using the Nose−Hoover thermostat with collision frequency set to 0.2 ps under *NVT* ensemble propagated by leapfrog integrator.[80] For the Drude force field, heating processes also employed *NVT* but utilized a dual-Langevin thermostat extended Lagrangian approach to propagate the dynamics.[81] The temperature of the Drude oscillators was set to 1.0 K with a collision frequency of 0.05 ps, while the temperatures of real atoms were set accordingly. The maximum distance between Drude oscillators and their core atoms is set to 0.25 Å as a HARDWALL to prevent them from straying too far during the simulations. After heating, 100 *ns NPT* production runs were carried out using OpenMM 7.3.0[82,83] for both C36m and Drude force fields with the same conditions in the *NVT* simulations except that the pressure is set to 1 bar. The analysis is based on the trajectories obtained from both force fields during the last 80 ns *NPT* simulations unless otherwise specified. Visualizations were achieved by VMD 1.9.3.[84]

2.3. GCMC Simulations and Analysis. To investigate the distribution of water molecules inside the FFPNTs and their capability to hold water, we carried out GCMC/MD simulations. The hexagonal crystal unit was first cut into an orthorhombic crystal unit, as illustrated by the red rectangle in Figure 1b. Five layers (60 FFs) were included, with the crystal parameters of a = 24.0709 Å, b = 41.691 Å, c = 27.280 Å, α = 90°, β = 90°, and γ = 90°. In this trimmed system, 100 water molecules were randomly placed in the channel as the initial condition for carrying out GCMC simulations. We note that the number of initial water molecules will not influence the final results of GCMC simulations; however, placing some initial water molecules helps accelerate the sampling and convergence of GCMC compared to using an empty channel. The systems were equilibrated with 10 ns *NVT* and 10 ns *NPT* MD simulations with C36m and Drude force fields to obtain an initial state for the GCMC simulations.

GCMC/MD simulations were carried out with an in-house code that interfaces with CHARMM for better control of the Drude force field. The code was validated using a bulk water system with either the TIP3P or SWM4-NDP water model (see the Supporting Information for more details). The code was made open source and can be accessed at https://github.com/JingHuangLab/gcbgcmc. In the GCMC implementation, three equally likely move instances occurred: rigid displacement, creation, and annihilation of water molecules, following the strategy proposed by Mezei.[85] Furthermore, we adopted Adams's strategy that introduces a B parameter instead of the chemical potential (μ) to control the probability of inserting or deleting water molecules.[86] The sampling efficiency of insertion in GCMC was enhanced by employing a grid cavity-biased strategy proposed by Mezei.[85] The GCMC region was a 10 × 10 × 25 Å^3 cuboid box, and the grid employed in our work was periodic along only the Z-axis. The length of each grid lattice is set to 0.25 Å, and the cutoff radius (r_{cut}) for determining whether a grid is considered a cavity was set to 2.5 Å. Specifically, for the Drude force field, before each GCMC step was justified for acceptance, 5 steps of steepest decent (SD) minimization were performed to relax only the Drude oscillators, while the grid information was also updated. Due to the lack of knowledge of a proper B parameter, the GCMC/MD simulations followed an elegant protocol proposed by Ross et al.,[37,87] which is similar to performing titration experiments. Briefly, a set of GCMC/MD simulations was carried out at a range of B parameters to titrate the N_w in the pore of FFPNTs.[37] At 150 K, for C36m, the range of Adams factor B was adopted between [−50, 0] with an increment of 1, while for Drude, Adams's parameter B ranged in [−20, 20] with an increment of 1. At 298.15 K, for C36m, B ranged in [−10, 5] with an increment of 0.5, and for Drude B ranged [−10, 20] with an increment of 1. For both C36m and Drude force fields, at each B value, we performed 5 replicas of GCMC/MD simulations. Each replica had 5 × 10^5 GCMC movements, and after every 500 GCMC steps, a 500-step *NVT* MD (time step of 1 fs) was performed at the corresponding temperature. CHARMM was used for performing the MD simulations, with details the same as those in the previous MD section. Snapshots of GCMC/MD simulations were saved after each combination of 500 steps of GCMC and 500 steps of MD simulations. A total of 1000 frames were saved for each run with a given B parameter. The SHAKE algorithm was employed as described previously, and no additional constraints or restraints were applied to the GCMC/MD simulations.

The results of GCMC/MD will be analyzed similarly to the proposed grand canonical integration by Ross et al.[37,87] The relationship between the number of water molecules (N_w) and the B value is fitted into a sum of logistic functions

$$N_w(B) = \sum_{i=1}^{m} \frac{n_i}{1 + \exp(w_{0i} - w_i B)} \quad (1)$$

where the parameters m, n_i, w_{0i}, and w_i are fitted. The parameter m is evaluated by the approximate number of "steps" of the titration curve. The parameter n_i is the number of waters coupled in step i, while w_{0i} and w_i are the point of inflection of the logistic curve i and its steepness, respectively. The GCMC results are analyzed with the aid of ProtoMS (version 3.4).[88] The fitted curve can reveal the distribution of water molecules inside the FFPNTs at different states as a result of the varying B parameters.

3. RESULTS

3.1. Structure of FFPNT under Different Hydration States with MD Simulations. We first performed MD simulations with different hydration state conditions to study the impact of water molecules on the structure of FFPNT. Seven different hydration states were set up, and simulations were carried out under two temperatures, 150 and 298.15 K. It was found that FFPNTs can accommodate a large number of water molecules, as the only crashed simulation was for the Sys_9 at 298.15 K with the Drude force field, where too many water molecules were close to each other inducing the polarization catastrophe. Examination of the root-mean-square deviations (RMSDs) of heavy atoms with respect to the crystal structure showed significantly larger RMSDs for the Sys_9 and Sys_5 systems at 150 K (Table S1 and Figures S2−S5), indicating that these systems underwent larger structural deformation compared to others.

These observations are more pronounced at 298.15 K, where the RMSDs were small and indistinguishable from each other for systems containing no more than 3 water molecules per FF, while systems with more water exhibit larger RMSDs of FF molecules. Closer inspection of the structures reveals that the nanotube structure can indeed be disrupted when too

https://doi.org/10.1021/acsomega.3c06071
ACS Omega 2023, 8, 42936−42950

many water molecules are present inside, and the excess water is leaking out of the channel (Figures S6–S7). Comparing the two force fields, RMSDs obtained from Drude simulations were consistently lower than the corresponding C36m simulations, indicating the interactions modeled by the Drude force field are in general stronger.

The stability of FFPNTs relies critically on the hydrogen bond (H-bond) network formed among the FFs themselves and between FFs and water molecules. To this end, we analyzed the number of H-bonds (N_{HB}) formed among each FF (N_{HB}^{FF}) and between the FFs and water (N_{HB}^{FW}). The averaged N_{HB} for each MD frame was computed using the criteria proposed by Baker and Hubbard (θ > 120° and $R_{H\cdots acceptor}$ < 2.5 Å).[89] As shown in Figure 2, N_{HB}^{FF} per FF remains relatively constant at 3.8 and 3.3, respectively, for C36m and Drude force field when N_w is less than 5. Once N_w exceeds 5, N_{HB}^{FF} per FF decreases by about 23% in Sys_5 and 61% in Sys_9. In contrast, N_{HB}^{FW} exhibits opposite trends, with a dramatic increase to more than 5 per FF when N_w exceeds 4. This increase in N_{HB}^{FW} is expected to be halted once the bound water has been saturated. The analysis of N_{HB}^{FF} and N_{HB}^{FW} on different hydration states suggests that excessive water can destabilize the FFPNT structure, causing FFs to form H-bonds with water and other FFs in a competitive manner. At 298.15 K, these observations remain consistent, except that the Sys_4 system also demonstrates instability, likely due to higher water dynamics at an elevated temperature. In light of these results, the N_w inside the channel should be far less than the number of water sites (9) per FF resolved in the X-ray experiments, and some water sites cannot be occupied simultaneously. This discrepancy could be attributed to the crystal structure's unit cell being an average of a much larger supramolecule. Based on these analyses, we will focus on the systems with a reasonable N_w such that the channel structure of FFPNT is maintained, specifically Sys_0, Sys_1, Sys_2, and Sys_3.

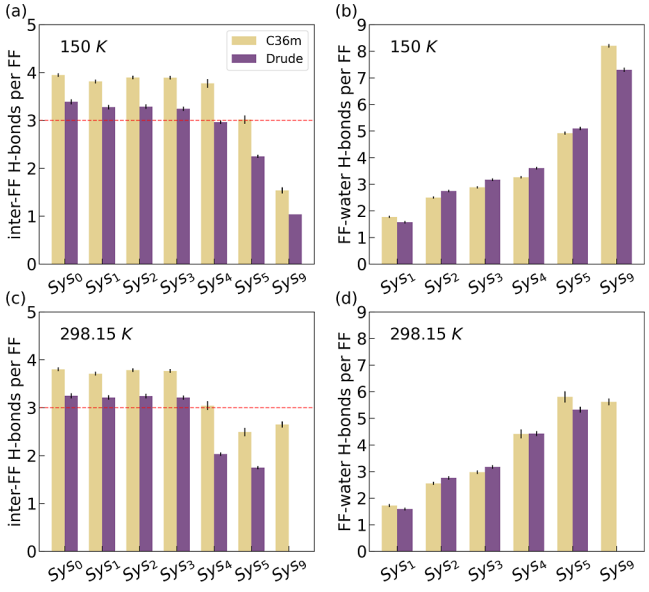

Figure 2. Number of H-bonds formed (a) between FFs (N_{HB}^{FF}) and (b) between FFs and waters (N_{HB}^{FW}) per FF at 150 K. Number of H-bonds formed (c) between FFs (N_{HB}^{FF}) and (d) between FFs and waters (N_{HB}^{FW}) per FF at 298.15 K. Standard deviations are plotted as error bars, and the red dashed lines in parts a and (c) show the number of hydrogen bonds in the crystal structure.

Furthermore, the number of H-bonds formed in FFPNT systems modeled by the two force fields exhibits systematic deviations. Both force fields estimate more N_{HB}^{FF} compared to the crystal structure (3 inter-FF H-bonds) when N_w is less than 4, with about 0.8 more H-bonds with C36m and 0.3 more with Drude. The smaller RMSDs associated with the Drude force field (as illustrated in Figures S6 and S6), along with N_{HB}^{FF} values resembling that of the crystal structure, suggest potential benefits of explicitly incorporating the polarization effect in modeling the FFPNT system. We note that employing Drude leads to fewer inter-FF H-bonds, but the interactions are stronger, as indicated by the smaller RMSD. The N_{HB}^{FW} is almost the same between these two force fields, suggesting an overestimation of the N_{HB}^{FF} in C36m. The additional H-bonds occurring in both C36m and Drude simulations are due to the rotation dynamics of the N terminal and the carboxyl group, which causes one of the H atoms to form two H-bonds with two O atoms instead of one in the crystal structure. Consequently, the additional H-bonds in C36m indicate that these H-bonds are weaker and less capable of maintaining the crystal structure, while the Drude shows some improvement in this regard. Furthermore, the number of H-bonds remains

Table 1. Average Lattice Sizes and Corresponding System Volumes Obtained from 80 ns *NPT* Trajectories of Each System with a Different N_w Value Simulated Using CHARMM Additive and Drude Polarizable Force Fields at 150 K[a]

	a (Å)	*b* (Å)	*c* (Å)	*V* (Å^3)
		CHARMM		
Sys_0	24.466(0.045)	24.467(0.030)	5.321(0.007)	2758.3(5.2)
Sys_1	24.470(0.050)	24.364(0.036)	5.332(0.010)	2752.8(5.5)
Sys_2	24.290(0.054)	24.357(0.033)	5.346(0.008)	2739.2(5.3)
Sys_3	24.424(0.060)	24.463(0.032)	5.353(0.008)	2769.9(5.3)
Sys_4	24.834(0.040)	24.776(0.029)	5.347(0.007)	2849.0(5.0)
		Drude		
Sys_0	24.159(0.048)	24.159(0.031)	5.429(0.007)	2744.3(5.1)
Sys_1	24.128(0.055)	24.002(0.035)	5.464(0.007)	2740.2(5.5)
Sys_2	24.014(0.044)	23.986(0.030)	5.463(0.007)	2725.1(5.0)
Sys_3	24.053(0.041)	24.051(0.028)	5.484(0.007)	2747.3(4.9)
Sys_4	24.236(0.046)	24.461(0.033)	5.543(0.008)	2845.7(5.2)
EXP	24.071	24.071	5.456	2737.7

[a]Also included are experimental values. Standard deviations are provided in parentheses.

https://doi.org/10.1021/acsomega.3c06071
ACS Omega 2023, 8, 42936−42950

unchanged at both temperatures, implying they are not sensitive to thermodynamic fluctuations.

We also computed the atomic root-mean-square fluctuations (RMSFs), converted these into *B* factors, and compared them to the crystallographically determined values at 150 K (see Supporting Information Section 4 for details). Due to the limitations in X-ray resolution to resolve the vibrations of hydrogen atoms, only heavy atom results were analyzed. Both force fields predicted smaller *B* factors for hydrated FFPNTs at 150 K, implying an overestimation of the atomic stability. The *B* factors derived from both force fields exhibited similar trends across different hydration states. In general, larger deviations were observed for the C36m simulations compared to those from the Drude simulations. We note that the Drude force field showed less vibration of the O than C36m, indicating stronger H-bonds in Drude, which aligns with our previous observations on N_{HB}^{FW}.

3.2. Anisotropic Stabilization Effects of Water. The crystal parameters obtained from the averaged hexagonal box sizes of each system from *NPT* simulations at 150 K were analyzed and compared with experimental measurements (Table 1). As the number of water molecules in the simulation system increased, the box size initially decreased and subsequently increased. For the C36m force field, the unit box size was smallest for Sys_2, at 2739.192 Å^3, while for simulations using the polarizable Drude force field, the unit box size was also smallest for Sys_2, at 2725.148 Å^3. These trends can be attributed to the fluctuating dimensions in the $x-y$ plane, which initially increases and then decreases with rising N_w. In contrast, the *c* length displays a consistently monotonic increase, exhibiting much less variation in response to changes in N_w. It is worth noting that the barostat was coupled to the MD system anisotropically, leading to distinct changes in the *a*, *b*, and *c* dimensions.

The reduction in the box size during crystal simulations indicates a stronger attraction between FFs. Furthermore, the specific alterations in the *a* and *b* dimensions as a function of N_w suggest that the water molecules aid in the stacking of FFPNTs along the $x-y$ plane. In a previous DFTB study, it was observed that the average interaction energy between water molecules and the FFPNT's inner wall first decreases and then increases with N_w, exhibiting a turning point at N_w = 3.3.[43] This study accounted for only a single hexamer unit (6 FFs) with PBCs, thereby assuming that the effects of water were exerted within the $x-y$ plane. Our results, obtained using a considerably larger simulation system (5 layers with 4 unit cells per layer, totaling 120 FFs), corroborated this assumption. It appears that confined water can help stabilize the $x-y$ plane while exerting a minimal influence on the *z* direction. Experimental findings from polarized Raman spectra provide further support for the significant impact of water on the transversal elastic constant of FFPNTs, while its influence in other directions remains minimal.[24] Our atomistic simulations suggested that the contribution of water to rigidity arises from the regular network of H-bonds formed by water molecules with the FF on the $x-y$ plane (see Figures S9 and S10). Notably, these radially oriented hydrogen bonds between FFs and water molecules are stronger than the inherent hydrogen bonding motifs between FFs in FFPNTs. This fact has also been elucidated experimentally through the refinement of electron density maps obtained from powder X-ray diffraction.[90]

With respect to the crystal parameter *c*, which aligns with the pore direction, a consistent but small increase was observed as N_w increased for both the additive CHARMM and the polarizable Drude force fields. While both force fields yielded results comparable to experimental measurements, the Drude force field generated smaller box sizes on the $x-y$ plane, bringing them closer to experimental outcomes. In terms of the crystal length along the pore direction, the Drude resulted in a longer length, aligned again better with experimental measurements compared to C36m, suggesting that the attraction between each layer of FFPNTs was modeled more accurately. The same trend was observed in simulations carried out at 298.15 K (Table S2).

3.3. Grand Canonical Simulations Indicate a Maximum Capacity of 2.6 Water Molecules per FF. MD simulations show that the nanotube structure composed of FFs can be severely damaged by an excessive number of water molecules inside, while a reasonable N_w value can stabilize the tube. To further investigate the optimal quantity and distribution of water molecules inside the FFPNT channel, we carried out GCMC/MD simulations with both the C36m and the Drude force fields at 150 and 298.15 K. Figure 3 presents the average N_w per FF across a range of Adams *B* parameters obtained from five independent GCMC/MD simulation replicas. As demonstrated in Figures S12−S20, a satisfactory degree of convergence has been achieved in each individual replica. However, we do note large variances across replicas in certain regions of the Adams *B* parameters. The hydration state of the FFPNT undergoes three distinct stages in response to changes in the *B* parameter, a pattern consistent across both force field models. Initially, the dehydrated state is characterized by a sparse presence of water molecules inside

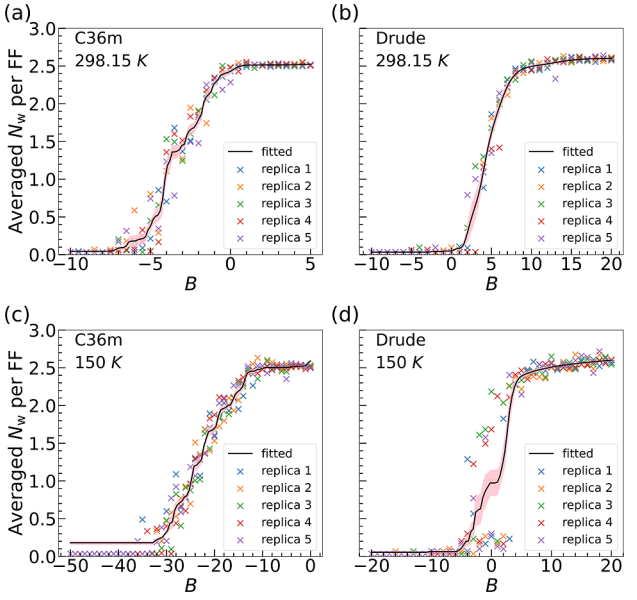

Figure 3. GCMC titration plot for water molecules in FFPNT channels obtained using (a) C36m at 298.15 K, (b) Drude at 298.15 K, (c) C36m at 150 K, and (d) Drude at 150 K, illustrating how the average number of the water molecules varies with the Adams *B* parameters. The black line of best fit is obtained through the least-squares fitting of eq 1 to N_w obtained from each replica GCMC (in colored cross symbols). The uncertainty of the fitted titration plot was estimated using 1000 bootstrap samples, and the 90% confidence interval of the bootstrap fits was plotted as the red-shaded region.

https://doi.org/10.1021/acsomega.3c06071
ACS Omega 2023, 8, 42936−42950

the channel. This is followed by the growing hydration state, during which the N_w value increases rapidly. Eventually, the saturation state is reached where the N_w stabilizes, signifying that the FFPNTs have achieved their maximum water molecule capacity of about 2.6 water molecules per FF.

In the hydration growing state, the variances of N_w per FF between the 5 replicate runs noticeably increase, a pattern that holds true across both FFs and various temperatures. Examination of the trajectories confirms that the nanotube structures remain stable, indicating that the observed variance arises from the limited sampling of water. Similar observations have been reported in previous GCMC studies[37,87] that proposed the fitting method, which we have also adopted in this work. Sampling with the Drude force field at 150 K (Figure 3d) was particularly challenging for three reasons. First, due to the high computational cost of achieving full self-consistent field (SCF) relaxation of Drude oscillators, we used a 5-step SD minimization to relax the Drude particles at each GCMC attempt. However, this approach does not guarantee the optimal positions of Drude particles to be the same as those in the SCF method, which can result in larger intermolecular forces within the system. Second, as previously discussed, the interactions between water and the peptide are stronger in the Drude force field. Third, the low temperature reduces the kinetics of the water molecules. The latter two factors both contribute to the difficulty in water movement when hydrogen bond networks are formed. Once such a network is established, water molecules are more readily inserted to form additional H-bonds and are less likely to leave. Conversely, if no strong hydrogen bond network is in place, water molecules move slowly and are more prone to be deleted in the GCMC moves. These factors collectively contribute to the large deviations observed across the different replicas.

With C36m at 298.15 K, the system predominantly remained in the dehydrated state when the B parameter was below −8. As the B parameter shifted into the interval of [−8, 0], the system transitioned to the hydration growing state, and the N_w dramatically increased from approximately 0 water molecules to around 2.5 per FF. Further increases in the B parameter drove the system into the converging state and slowly converged to approximately 2.6 per FF. Similar trends were observed with the Drude force field at 298.15 K. The system remained in the dehydrated state when B was less than 0. When B entered the [0, 8] range, the system transitioned into the hydration growing state. Upon exceeding 8, the B parameter shifted the system into the converging state. The first inflection point in the titration curves represents a preference for water molecules to enter the channel, reflecting a situation in which water molecules function as bound water and form hydrogen bond networks to stabilize FFPNTs. The second inflection point, indicating a higher probability of rejecting additional water insertion, represents the saturation of the channel. From this point on, inserting water molecules necessitates overcoming a higher energy barrier to become part of the system. At 150 K, the relationships mirrored those observed at 298.15 K, except that lower B values were required to reach the same states as in the 298.15 K simulations, and the hydration growing state proceeded at a slower rate. We note that the error bars during the hydration growing states were relatively large. The relationship between the Adams B factor and the excess chemical potential μ' is[86]

$$B = \mu'/k_BT + \ln \langle N \rangle \quad (2)$$

where $\langle N \rangle$ is the average number of particles in the GCMC region. When transforming μ' to the Adams parameter B, two points need to be mentioned concerning the additional Drude particles or Drude degrees of freedom (DOFs). First, the difference in DOFs between TIP3P and SWM4 water models is not relevant to insertion and deletion, as the number of DOFs cancels out when computing the probability of GCMC movements.[85] Second, the transformation from μ' to B is indeed influenced by the difference in the DOFs of the water models. This disparity impacts the ln $\langle N \rangle$ values, yielding a shift in the B parameters.

3.4. Comparison of Water Distribution and Occupancy. The water distribution within the channel obtained from GCMC/MD simulations at 150 K can be directly compared with the occupancy of each water site as determined by X-ray diffraction (Figure 2). A water site is considered occupied when the oxygen atom of a water molecule falls within a 1.25 Å cutoff distance (detailed in eq S1). The analysis was based on the last 300,000 steps of the GCMC/MD simulations (600 frames), with averages taken from the five replica runs. As the total number of water occupancy from the X-ray experiment equals 2.473 per FF,[1] we calculated water site occupancy from the GCMC/MD simulations carried out at B = −12 for the C36m model (yielding N_w = 2.452 per FF) and at B = 6 for the Drude model (yielding N_w = 2.496 per FF). To account for the fact that not all simulation waters can be attributed to the experimental water sites, we also computed the proportional occupancy (r_O), defined as the occupancy of each water site divided by the total N_w per FF.

The calculation results reproduce the general trend that the absolute occupancy of these water sites is low (less than 0.4), thus underscoring the highly dynamic nature of the confined water (Table 2). Using the C36m force field, the proportional occupancy at water sites "O1C", "O1F", "O1H", and "O1J" were found to be notably weaker than experimental values, yielding 0.031, 0.071, 0.022, and 0.027, respectively. We note that "O1C", "O1F" and "O1J" have the highest experimental occupancy values among the nine sites, with r_O being 0.155, 0.133, and 0.153, respectively. The "O1C" and "O1F" sites, located close to $-COO^-$ and $-NH_3^+$, respectively, correspond to bound water that is supposed to be particularly stable within the hydrogen bonding networks. Meanwhile, the "O1J" site

Table 2. Water Site Occupancy and Relative Proportion (r_O) Obtained from GCMC/MD Simulations Employing the C36m and Drude Force Fields at 150 K

	C36m		Drude		Expt.	
water sites	occupancy	r_O	occupancy	r_O	occupancy	r_O
O1C	0.077	0.031	0.186	0.075	0.383	0.155
O1D	0.314	0.128	0.220	0.088	0.206	0.083
O1E	0.297	0.121	0.207	0.083	0.275	0.111
O1F	0.174	0.071	0.267	0.107	0.329	0.133
O1G	0.279	0.114	0.036	0.014	0.253	0.102
O1H	0.054	0.022	0.126	0.050	0.235	0.095
O1I	0.344	0.140	0.192	0.077	0.267	0.108
O1J	0.067	0.027	0.220	0.088	0.378	0.153
O1K	0.172	0.070	0.160	0.064	0.147	0.059
sum	1.778	0.725	1.614	0.647	2.473	1.000
total	2.452		2.496		2.473	
RMSE		0.070		0.050		

https://doi.org/10.1021/acsomega.3c06071
ACS Omega 2023, 8, 42936−42950

represents free water that directly interacts with bound water. In contrast, the proportional occupancy for the "O1D" and "O1I" sites was found to be 0.128 and 0.140 with the C36m force field, both significantly overestimated compared to the experimental data. These two sites are located near the head-to-tail terminal and can form H-bonds simultaneously with $-COO^-$ and $-NH_3^+$. Another overestimated site, "O1E" is located between the $-NH_3^+$ and $-COO^-$ of the same FF and can act as both a proton donor and acceptor, enabling the formation of H-bond networks.

Using the Drude force field, the proportional occupancies (r_O) of water sites "O1C", "O1F" and "O1J" were approximately 1.5 to 3 times larger than those derived from the C36m simulations yet still did not reach the experimental occupancy levels. Moreover, all 9 water sites exhibited occupancies that were either comparable to or lower than the experimental data. We note that the "O1C" and "O1D" sites are in close proximity to each other with nearly identical x and y coordinates and a mere ~0.8 Å separation in the z direction. This might introduce some ambiguities in assigning their respective water occupancies. Nevertheless, this particular set of experimental data presents a substantial and challenging test case for benchmarking protein force fields and water models.

To visualize the water distribution, we depicted the density profiles of the oxygen atoms of confined water molecules projected onto the $x-y$ plane (Figures S21−S29). Both the C36m and Drude force fields led to a clear hexagonal structure, which can be attributed to the interactions between water and the hydrophilic groups. As N_w increased, the water molecules initially filled as bound water and gradually congregated in the central region. The C36m simulations resulted in more continuous density profiles, while the Drude simulations generated relatively more discrete ones. This discrepancy might suggest that the interactions between FFPNTs and water were stronger in the Drude polarizable force field. Moreover, the Drude force field yielded a more uniform water position distribution, indicating potentially more effective sampling. Our results demonstrated more continuity compared to the previous study using DFTB-level MD simulations on a much smaller FFPNT unit cell,[43] likely due to the more realistic modeling of the system as well as the much longer simulation times in our study.

3.5. Water Transport in the FFPNT Channel. We next analyze the water transport in the FFPNT channel. From earlier discussions, it is clear that there are two types of water molecules in the channel. To distinguish between free and bound water molecules, radial distribution functions (RDFs) of water oxygen atoms relative to the terminal N atoms were calculated using MD trajectories at 298.15 K. Additionally, extra MD trajectories for $Sys_{2.5}$ were generated, as this might better represent hydrated FFPNTs based on our GCMC/MD results. In general, the RDFs displayed a pronounced and narrow first peak for both force fields (Figure 4). It was also observed that the peak from C36m was positioned further than that from the corresponding Drude force field, indicating that the attractions between water and FF are stronger with Drude. Accordingly, a distance of 3.2 Å was established to differentiate between free and bound water for the C36m force field and a distance of 3.0 Å for Drude.

When we computed the MSDs of water molecules along the pore (z) direction without differentiating between bound and free water, water motion appeared to follow the Fickian-type

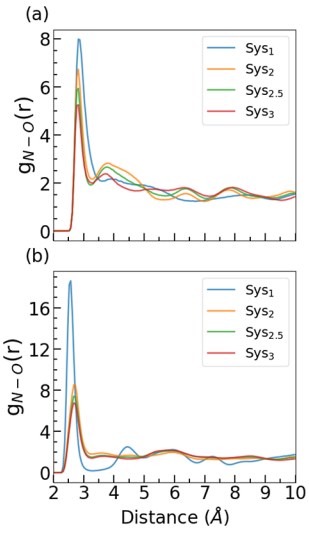

Figure 4. RDFs of the water oxygen atoms with respect to the FF terminal N atoms, derived from the last 80 ns trajectories of C36m simulations (a) and Drude simulations (b) at 298.15 K.

transport as shown in Figure 5a,d. Using the Einstein relationship, we determined the diffusion coefficients to be 1.211×10^{-9} m^2/s for the $Sys_{2.5}$ system with C36m and 0.625×10^{-9} m^2/s with Drude, respectively. Subsequent analysis on the residence time of free and bound water (Figure S32), however, demonstrated that both types of water molecules persisted only for short durations (less than 50 ps). Such rapid interchange between the two states emphasized the necessity of distinguishing between them when studying water transport in FFPNTs. To this end, we calculated the diffusion coefficient ($\mathcal{D}$) of water in the FFPNT channel according to the method proposed by Liu et al. specifically for confined fluids[91,92]

$$\mathcal{D} = \lim_{\tau \to \infty} \frac{\langle \Delta z(\tau)^2 \rangle}{2\tau P(\tau)} \tag{3}$$

where the MSD of water along the pore direction ($\langle \Delta z^2(t) \rangle$) was computed considering its survival probability $P(\tau)$ in its own type. Detailed equations for calculating $\langle \Delta z^2(t) \rangle$ and $P(\tau)$ can be found as eqs 14 and 15 in ref 91. The computed MSDs are plotted against τ in Figure 5 and the diffusion coefficients are listed in Table 3.

The transport behaviors and diffusion coefficients of bound and free water exhibited notable differences. For bound water (Figure 5b,e), both force fields resulted in similar single-file transport behavior. This could be attributed to the hydrogen bonding network between water and FF, as the bound water molecules were more likely to move through the formation and disruption of H-bonds in a highly coordinated manner, thereby following single-file transport. In contrast, free water displayed a varied behavior contingent on both N_w and the chosen force field. With C36m, free water molecules in Sys_2 behave as a single-file type while in $Sys_{2.5}$ and Sys_3 the water molecules follow the Fickian-type transport. With Drude, the free water in Sys_2 behaves more like the ballistic type while in $Sys_{2.5}$ and Sys_3 is more likely to follow the Fickian-type transport. The scenario where $N_w = 2$ was intriguing because it represented a situation with a limited number of free water molecules. The ballistic-type transport in Sys_2 might have been caused by the effective repulsion between water molecules and vacuum space that renders these free water molecules move faster.

https://doi.org/10.1021/acsomega.3c06071
ACS Omega 2023, 8, 42936−42950

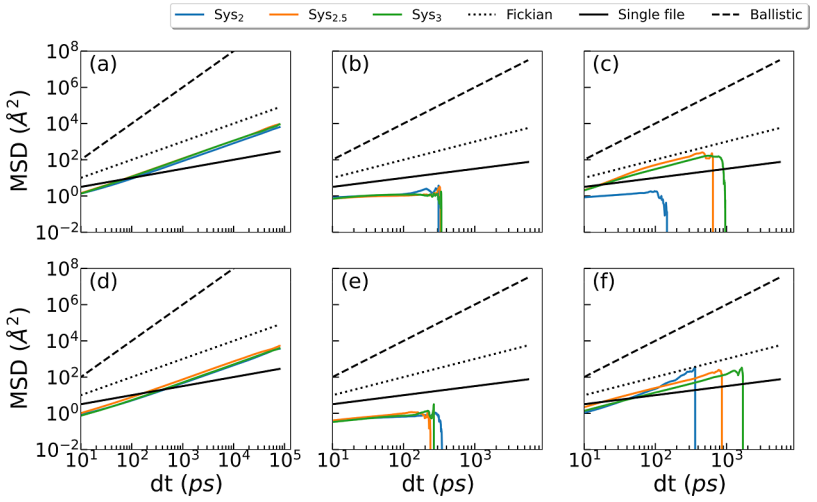

Figure 5. Mean square displacements along the pore direction as a function of time for the systems with 1, 2, 2.5, and 3 water molecules per FF at 298.15 K. (a) MSDs of all water molecules from C36m (b) MSDs of bound water molecules from C36m (c) MSDs of free water molecules from C36m (d) MSDs of all water molecules from Drude (e) MSDs of bound water molecules from Drude (f) MSDs of free water molecules from Drude. The solid, dashed, and dotted black lines illustrate the standard scaling for single-file, ballistic, and Fickian-type transport, respectively.

Table 3. Diffusion Coefficients for Free and Bound Water Molecules in Systems with 1, 2, 2.5, and 3 Water Molecules Per FF Employing Both the C36m and Drude Force Fields at 298.15 K[a]

	C36m		Drude	
	bound	free	bound	free
Sys_1	0.685	0.103	0.017	0.429
Sys_2	0.053	0.104	0.034	2.195
$Sys_{2.5}$	0.044	5.554	0.069	2.548
Sys_3	0.064	3.189	0.052	1.398

[a]The unit is in 10^{-9} m^2/s.

In terms of diffusion coefficients, 2 orders of magnitude differences were observed between the two types of water. The bound water molecules were severely retarded due to the hydrogen bond networks with the hydrophilic walls. Their diffusion coefficients were about 0.05×10^{-9} m^2/s, insensitive to N_w. In contrast, the $\mathcal{D}$ values of free water molecules varied according to the hydration level. Interestingly, for $Sys_{2.5}$ the diffusion coefficients were similar to those of bulk water, 5.72×10^{-9} m^2/s and 2.57×10^{-9} m^2/s for the TIP3P and SWM4 water model, respectively. This suggests that the bound water surrounding free water molecules provides an environment very similar to that of bulk water for both additive and polarizable force fields. Either smaller or larger at N_w resulted in slower transport of the free water. We note that one experiment reported $\mathcal{D} = 0.13 \times 10^{-9} m^2/s$ for the confined water in FFPNT at 30 °C and relative humidity at 38% using FFPNTs constructed with D, D-FFs.[26] For water transport properties, D, D-FFs and L, L-FFs should be the same since the dominant hydrophilic interior walls and hydrophobic phenyl rings are in the same location. The general slowdown in water diffusion rate in the FFPNT is consistent with previous studies on hydrophilic-groups-dopped single-wall CNTs.[93,94]

3.6. Polarization Leads to More Realistic Behavior of FFPNTs and Water. Employing a polarizable force field model enabled us to profile the polarization effects in the FFPNT systems. Electronic polarization has been reported to be important for water molecules confined in CNTs,[46] but it has not been studied in detail for peptide nanotubes. Here, we analyzed the dipole moments of water and amino acids along the 298.15 K MD trajectories using CHARMM. Figure 6 presents the distribution of water dipole moments for different hydration states. In Sys_1, waters were already highly polarized by the FFPNTs, as indicated by a peak centered at 2.37 D. As N_w increased, the distribution of water dipole moments shifted higher and became closer to that of the SWM4 bulk water, which was derived from *NPT* simulations using a water box of $34 \times 34 \times 34$ $Å^3$ at 298.15 K and 1 atm. The distribution of Sys_2 was more skewed compared to the SWM4 bulk water, with a higher proportion of water molecules having smaller dipoles (between 2.0 and 2.25 D), suggesting a more complicated and inhomogeneous electrostatic environment in nanotubes. In addition, no significant difference between the dipole distributions of bound water and free water was observed (Figure S30), which indicates that both types of water share a similar electrostatic environment shaped by the FFPNTs and the water molecules themselves. We note that in all additive simulations, the dipole moment of water molecules was fixed at 2.35 D.

Since the dipole is a vector, we further analyzed the distributions of water dipole orientation represented by the cosine of the angle ($\cos\theta$) between the water dipole and the *z*-axis (Figure 7). In Sys_1, the majority of water molecules existed as bound water and displayed dipoles oriented almost opposite to the *z*-axis due to their strong interactions with the FFPNTs ($\cos\theta \approx -1$). Notably, the Drude force field results in a significantly more pronounced orientation in this direction compared to C36m. With the additive force field models, the alignment of dipole moments can only be achieved by the geometric rotation of waters, while with the polarizable force field models, the induced dipole can more easily facilitate the alignment of total dipole moments along the desired directions.

In Sys_2, C36m yielded a distribution with orientations primarily normal to the nanotube wall ($\cos\theta \approx 0$), while Drude exhibited a bimodal distribution with nearly equal proportions of orientations normal to the wall and those opposite the pore. As N_w increased, the preference for any

https://doi.org/10.1021/acsomega.3c06071
ACS Omega 2023, 8, 42936−42950

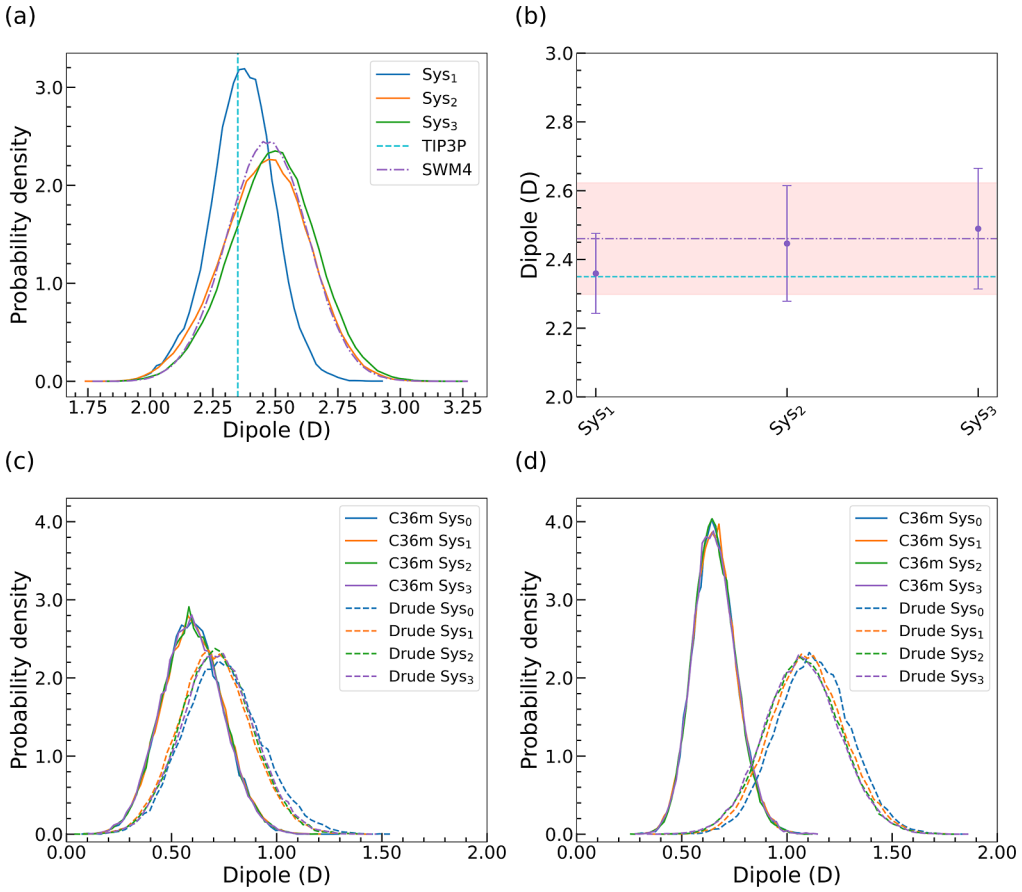

Figure 6. (a) Dipole moment of water molecules inside the FFPNTs and SWM4-NDP water in bulk as well as the TIP3P water model. (b) Average water dipole moment of each system. The dipole moment of TIP3P water and bulk SWM4-NDP are plotted with dashed line and dash-dot line, respectively. The red-filled region is the standard deviation. (c) Dipole moment of the side chain of the FFs in the vicinity of the N terminal simulated by C36m and Drude force fields. (d) Dipole moment of the side chain of the FFs in the vicinity of the C terminal simulated by C36m and Drude force fields.

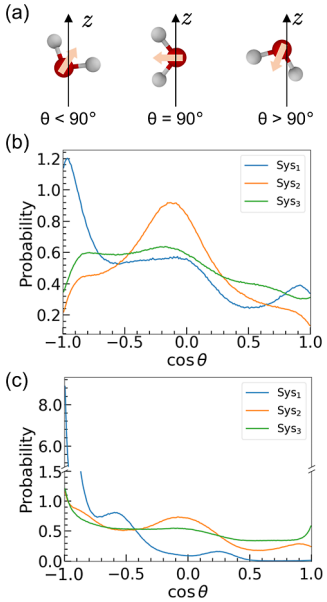

Figure 7. (a) Illustration of water dipole orientation. (b) Distribution of water orientation in the system simulated with the C36m force field at 298.15 K. (c) Distribution of water orientation in the system simulated with the Drude force field at 298.15 K.

particular dipole orientation diminished, suggesting that additional water molecules counteracted the influence of FFPNTs. The divergence in results between C36m and the Drude force field became less pronounced with increasing N_w, implying that employing a mean-field approach to capture the polarization effect was appropriate when modeling scenarios with the presence of more water.

The dipole moments of the FF side chains were also analyzed and are depicted in Figure 6c,d. The two phenylalanine side chains in each FF exhibited distinct dipole distributions. For clarity, the side chain in the vicinity of the N terminal is termed the "first side chain" and the one in the vicinity of the C terminal is termed the "second side chain". With both force field models, the dipole moments of the second side chains were higher than the first ones, though the magnitude of this difference varied. With C36m, the mean dipole values for the first and second side chains were 0.6 and 0.7 D, respectively. In contrast, the distribution peaked at 0.7 and 1.2 D in the Drude simulations. The observed capability of the Phe side chains to manifest greater dipole moments and exhibit variations based on their environment with the Drude force field aligns with prior findings from solvated protein simulations (as seen in Figure S2F in ref 95).

https://doi.org/10.1021/acsomega.3c06071
ACS Omega 2023, 8, 42936−42950

4. CONCLUSIONS AND DISCUSSION

In this study, we employed MD and state-of-the-art GCMC/MD simulations to systematically investigate the structure and dynamics of FFPNTs, with a particular focus on the behavior of water molecules confined within, using both the C36m additive and Drude polarizable force fields. The relative simplicity of the system, encompassing only water and a single type of amino acid, allowed for long timescale simulations and detailed analyses of the interactions in this system. Our MD results show that the FFPNTs modeled with the Drude force field are more stable and more consistent with the X-ray-determined structure than those modeled with the C36m force field. Additionally, the Drude force field has improved the overestimation of N_{HB}^{FF} in comparison to the C36m force field, though a slight overestimation persists. Notably, while nine water sites were identified in the crystal structure, the simulation results showed that all of these water sites are partially occupied. Furthermore, a reasonable number of confined water molecules helps stabilize the FFPNTs on the $x-y$ plane.

Through GCMC/MD simulations using both the C36m and Drude force fields, we established that the nanotube can accommodate 2.6 water molecules per FF. These findings examine the damage of FFPNTs by more than 3 water molecules per FF in the MD simulations, providing the basis for further determining the reasonable number of water molecules in FFPNTs. The occupancies of experimentally resolved water sites from the simulations were also compared to experimental results. The relationship between the Adams B parameter and the N_W delineated in this work can be employed to bridge the experimental conditions and N_W in FFPNT, serving as a reference for controlling N_W under experimental conditions, thereby facilitating the utilization of specific properties of FFPNTs such as their strong piezoelectricity. Kinetic analyses from MD trajectories provided insights into the transport behaviors of the confined water molecules. Bound water molecules in FFPNTs exhibit single-file transport, while free water molecules follow Fickian-type diffusion, which remained consistent across both force field models. Although free and bound waters were found to frequently interchange within the picosecond time scale, the exchange had a minimal effect on diffusion. These findings, based on simulations with a relatively large system and a long time scale, offer valuable reference points for deepening the understanding of water behavior under confinement. Alongside further investigations into the behavior of small molecules in FFPNTs, these diffusion characteristics can inform the modification of FFPNTs for use as a biocompatible drug delivery biomaterial. Moreover, given the intrinsic connection between these confined water molecules and the piezoelectricity of FFPNTs,[3] our findings provide a foundational basis for future simulations investigating the potential of FFPNTs as viable biosensors.

The slowdown of water diffusion in hydrophilic-wall CNTs has been attributed to two competing processes "cluster-breakage" and "cluster-libration", with the former facilitating faster transport than the latter.[93] Although in this study the CNTs were modified with 8 carbonyl groups on the interior walls, which did not constitute realistic systems, their results can be generalized and applied in nanotubes with hydrophilic walls. In the case of FFPNTs, the hydrophilic groups in their interior walls can form strong hydrogen bond networks that inhibit the "cluster-libration" process. This results in the immobilization of bound water while simultaneously slowing the movement of free water and preventing the formation of water clusters that move coherently. Even though there is a frequent exchange between the bound and free water, as suggested by their residence times, this exchange does not directly impact the transport mechanism. The hydration states also play a role in water transport behaviors as well. Our GCMC/MD simulations suggest that water molecules initially wet the FFPNT's internal wall and move slowly as bound water. As N_w increases, free water molecules appear which can migrate along the pore axis. The hydrophilic functional groups within FFPNTs may also interact with other small molecules such as small drug molecules or ions. In particular, the bound water provides an electrostatic environment similar to that of bulk water, supporting the subsequent exploration of FFPNTs as models for natural ion channels.

The present work supports the idea that the Drude polarizable force field, which explicitly includes polarization via the classical Drude oscillator model, is suitable for studying peptide nanotubes and their confined water molecules. Further dipole moment analyses from MD simulations revealed that the Drude force field produced more realistic dipole behaviors as both the magnitude and the orientation of dipole moments could respond more effectively to their environment. Our findings align with previous studies on protein folding which reported improved interactions between proteins and water molecules with the Drude model.[96] However, for many observables, we obtained similar results between the additive CHARMM force field and the polarizable Drude force field models, for example, the transport kinetics of confined water molecules. This similarity was also observed in QM/MM studies that reported minimal differences in energy barriers and reaction energies (0.5−1.5 kcal/mol) between CHARMM and Drude models serving for the MM part in systems ranging from water trimers to complex enzymatic reactions.[97,98] It seems that current state-of-the-art additive force fields can offer reasonably accurate modeling using mean-field average approximation,[99] even for challenging systems like the FFPNTs discussed here. Probably, the importance of explicit inclusion of electronic induction will be highlighted in the presence of a stronger electrostatic field.[62,67,100]

We considered the water distribution and occupancy inside the peptide nanotubes as critical observables to assess force field models. Both force fields exhibited similar discrepancies when compared to the experimental water occupancies. Notably, most water models are parametrized to reproduce the properties of bulk water, and their performance under nanoconfined conditions remains a subject of debate.[101] The SWM4 water model, used in the current Drude force fields, might not excel at reproducing the energetics and geometries of water clusters.[56,102] We anticipate that the application of the Drude force field in both MD and GCMC/MD simulations can be extended to other PNTs. This would enable more realistic modeling of water molecules or other small molecules under nanoconfined conditions, such that simulations could contribute to advancing the applications of PNT-based biomaterial. It is also important to note that due to the extremely high computational cost associated with the SCF relaxation of Drude oscillators, we adopted 5-step minimization instead of SCF to relax the Drude particles during the GCMC steps, which does not guarantee the minimization of intermolecular forces in the system and can result in poor sampling when using the Drude force field. For the broader

https://doi.org/10.1021/acsomega.3c06071
ACS Omega 2023, 8, 42936−42950

application of the Drude polarizable force fields, further refinement of parameters[60,103] and theoretical exploration[104,105] would be essential.

■ ASSOCIATED CONTENT

Supporting Information

The following files are available free of charge. The Supporting Information is available free of charge at https://pubs.acs.org/doi/10.1021/acsomega.3c06071.

RMSD plots along the MD simulations, RMSFs of heavy atoms at 150 K, validation of the in-house GCMC program, convergence of GCMC/MD simulations, and residence time of bound and free water (PDF)

■ AUTHOR INFORMATION

Corresponding Author

Jing Huang − *Key Laboratory of Structural Biology of Zhejiang Province, School of Life Sciences, Westlake University, Hangzhou, Zhejiang 310024, China; Westlake AI Therapeutics Lab, Westlake Laboratory of Life Sciences and Biomedicine, Hangzhou, Zhejiang 310024, China;* orcid.org/0000-0001-9639-2907; Email: huangjing@westlake.edu.cn

Authors

Jinfeng Chen − *College of Life Sciences, Zhejiang University, Hangzhou, Zhejiang 310027, China; Key Laboratory of Structural Biology of Zhejiang Province, School of Life Sciences, Westlake University, Hangzhou, Zhejiang 310024, China; Westlake AI Therapeutics Lab, Westlake Laboratory of Life Sciences and Biomedicine, Hangzhou, Zhejiang 310024, China;* orcid.org/0009-0008-8152-5672

Zongyang Qiu − *Key Laboratory of Structural Biology of Zhejiang Province, School of Life Sciences, Westlake University, Hangzhou, Zhejiang 310024, China; Westlake AI Therapeutics Lab, Westlake Laboratory of Life Sciences and Biomedicine, Hangzhou, Zhejiang 310024, China*

Complete contact information is available at: https://pubs.acs.org/10.1021/acsomega.3c06071

Notes

The authors declare no competing financial interest.

■ ACKNOWLEDGMENTS

The authors thank Dr. Xiang Yu for the helpful discussions. The work is supported by the "Pioneer" and "Leading Goose" R&D Program of Zhejiang (2023C03109), the National Natural Science Foundation of China (32171247, 21803057), the Zhejiang Provincial Natural Science Foundation of China (LR19B030001), the China Postdoctoral Science Foundation (2020M681934), and the Westlake Education Foundation. We thank Westlake University Supercomputer Center for computational resources and related assistance.

■ REFERENCES

(1) Görbitz, C. H. Nanotube Formation by Hydrophobic Dipeptides. *Eur. J. Chem.* **2001**, *7*, 5153−5159.

(2) Kol, N.; Adler-Abramovich, L.; Barlam, D.; Shneck, R. Z.; Gazit, E.; Rousso, I. Self-Assembled Peptide Nanotubes Are Uniquely Rigid Bioinspired Supramolecular Structures. *Nano Lett.* **2005**, *5*, 1343−1346.

(3) Kholkin, A.; Amdursky, N.; Bdikin, I.; Gazit, E.; Rosenman, G. Strong Piezoelectricity in Bioinspired Peptide Nanotubes. *ACS Nano* **2010**, *4*, 610−614.

(4) Matos, I. d. O.; Alves, W. A. Electrochemical Determination of Dopamine Based on Self-Assembled Peptide Nanostructure. *ACS Appl. Mater. Interfaces* **2011**, *3*, 4437−4443.

(5) Bianchi, R. C.; da Silva, E. R.; Dall'Antonia, L. H.; Ferreira, F. F.; Alves, W. A. A Nonenzymatic Biosensor Based on Gold Electrodes Modified with Peptide Self-Assemblies for Detecting Ammonia and Urea Oxidation. *Langmuir* **2014**, *30*, 11464−11473.

(6) Ghadiri, M. R.; Granja, J. R.; Milligan, R. A.; McRee, D. E.; Khazanovich, N. Self-assembling organic nanotubes based on a cyclic peptide architecture. *Nature* **1993**, *366*, 324−327.

(7) Ghadiri, M. R.; Granja, J. R.; Buehler, L. K. Artificial transmembrane ion channels from self-assembling peptide nanotubes. *Nature* **1994**, *369*, 301−304.

(8) Azriel, R.; Gazit, E. Analysis of the Minimal Amyloid-forming Fragment of the Islet Amyloid Polypeptide. *J. Biol. Chem.* **2001**, *276*, 34156−34161.

(9) Mazor, Y.; Gilead, S.; Benhar, I.; Gazit, E. Identification and Characterization of a Novel Molecular-recognition and Self-assembly Domain within the Islet Amyloid Polypeptide. *J. Mol. Biol.* **2002**, *322*, 1013−1024.

(10) Reches, M.; Porat, Y.; Gazit, E. Amyloid Fibril Formation by Pentapeptide and Tetrapeptide Fragments of Human Calcitonin. *J. Biol. Chem.* **2002**, *277*, 35475−35480.

(11) Lemkul, J. A.; Huang, J.; MacKerell, A. D. J. Induced Dipole-Dipole Interactions Influence the Unfolding Pathways of Wild-Type and Mutant Amyloid β-Peptides. *J. Phys. Chem. B* **2015**, *119*, 15574−15582.

(12) Brahmachari, S.; Arnon, Z. A.; Frydman-Marom, A.; Gazit, E.; Adler-Abramovich, L. Diphenylalanine as a Reductionist Model for the Mechanistic Characterization of β-Amyloid Modulators. *ACS Nano* **2017**, *11*, 5960−5969.

(13) Seabra, A. B.; Durán, N. Biological applications of peptides nanotubes: An overview. *Peptides* **2013**, *39*, 47−54.

(14) Hamley, I. W. Peptide Nanotubes. *Angew. Chem., Int. Ed.* **2014**, *53*, 6866−6881.

(15) Adler-Abramovich, L.; Reches, M.; Sedman, V. L.; Allen, S.; Tendler, S. J. B.; Gazit, E. Thermal and Chemical Stability of Diphenylalanine Peptide Nanotubes: Implications for Nanotechnological Applications. *Langmuir* **2006**, *22*, 1313−1320.

(16) Noy, A.; Park, H. G.; Fornasiero, F.; Holt, J. K.; Grigoropoulos, C. P.; Bakajin, O. Nanofluidics in carbon nanotubes. *Nano Today* **2007**, *2*, 22−29.

(17) Esin, A.; Baturin, I.; Nikitin, T.; Vasilev, S.; Salehli, F.; Shur, V. Y.; Kholkin, A. L. Pyroelectric effect and polarization instability in self-assembled diphenylalanine microtubes. *Appl. Phys. Lett.* **2016**, *109*, 142902.

(18) Guo, C.; Luo, Y.; Zhou, R.; Wei, G. Probing the Self-Assembly Mechanism of Diphenylalanine-Based Peptide Nanovesicles and Nanotubes. *ACS Nano* **2012**, *6*, 3907−3918.

(19) Kumar, S.; Nussinov, R. Salt bridge stability in monomeric proteins 1 1Edited by J. M. Thornton. *J. Mol. Biol.* **1999**, *293*, 1241−1255.

(20) Azuri, I.; Adler-Abramovich, L.; Gazit, E.; Hod, O.; Kronik, L. Why Are Diphenylalanine-Based Peptide Nanostructures so Rigid? Insights from First Principles Calculations. *J. Am. Chem. Soc.* **2014**, *136*, 963−969.

(21) Perdew, J. P.; Burke, K.; Ernzerhof, M. Generalized Gradient Approximation Made Simple. *Phys. Rev. Lett.* **1996**, *77*, 3865−3868.

(22) Tkatchenko, A.; Scheffler, M. Accurate Molecular Van Der Waals Interactions from Ground-State Electron Density and Free-Atom Reference Data. *Phys. Rev. Lett.* **2009**, *102*, 073005.

(23) Niu, L.; Chen, X.; Allen, S.; Tendler, S. J. B. Using the Bending Beam Model to Estimate the Elasticity of Diphenylalanine Nanotubes. *Langmuir* **2007**, *23*, 7443−7446.

(24) Zelenovskiy, P.; Kornev, I.; Vasilev, S.; Kholkin, A. On the origin of the great rigidity of self-assembled diphenylalanine nanotubes. *Phys. Chem. Chem. Phys.* **2016**, *18*, 29681−29685.
(25) Jeon, J.; Mills, C. E.; Shell, M. S. Molecular Insights into Diphenylalanine Nanotube Assembly: All-Atom Simulations of Oligomerization. *J. Phys. Chem. B* **2013**, *117*, 3935−3943.
(26) Zelenovskiy, P. S.; Domingues, E. M.; Slabov, V.; Kopyl, S.; Ugolkov, V. L.; Figueiredo, F. M. L.; Kholkin, A. L. Efficient Water Self-Diffusion in Diphenylalanine Peptide Nanotubes. *ACS Appl. Mater. Interfaces* **2020**, *12*, 27485−27492.
(27) Nordquist, E. B.; Schultz, S. A.; Chen, J. Using Metadynamics To Explore the Free Energy of Dewetting in Biologically Relevant Nanopores. *J. Phys. Chem. B* **2022**, *126*, 6428−6437.
(28) Nittinger, E.; Flachsenberg, F.; Bietz, S.; Lange, G.; Klein, R.; Rarey, M. Placement of Water Molecules in Protein Structures: From Large-Scale Evaluations to Single-Case Examples. *J. Chem. Inf. Model.* **2018**, *58*, 1625−1637.
(29) Bucher, D.; Stouten, P.; Triballeau, N. Shedding Light on Important Waters for Drug Design: Simulations versus Grid-Based Methods. *J. Chem. Inf. Model.* **2018**, *58*, 692−699.
(30) Sun, D.; Lakkaraju, S. K.; Jo, S.; MacKerell, A. D. Determination of Ionic Hydration Free Energies with Grand Canonical Monte Carlo/Molecular Dynamics Simulations in Explicit Water. *J. Chem. Theory Comput.* **2018**, *14*, 5290−5302.
(31) Samways, M. L.; Bruce Macdonald, H. E.; Essex, J. W. grand: A Python Module for Grand Canonical Water Sampling in OpenMM. *J. Chem. Inf. Model.* **2020**, *60*, 4436−4441.
(32) Striolo, A.; Chialvo, A. A.; Gubbins, K. E.; Cummings, P. T. Water in carbon nanotubes: Adsorption isotherms and thermodynamic properties from molecular simulation. *J. Chem. Phys.* **2005**, *122*, 234712.
(33) Striolo, A.; Chialvo, A. A.; Cummings, P. T.; Gubbins, K. E. Simulated water adsorption in chemically heterogeneous carbon nanotubes. *J. Chem. Phys.* **2006**, *124*, 074710.
(34) Zheng, J.; Lennon, E. M.; Tsao, H.-K.; Sheng, Y.-J.; Jiang, S. Transport of a liquid water and methanol mixture through carbon nanotubes under a chemical potential gradient. *J. Chem. Phys.* **2005**, *122*, 214702.
(35) Vaitheeswaran, S.; Rasaiah, J. C.; Hummer, G. Electric field and temperature effects on water in the narrow nonpolar pores of carbon nanotubes. *J. Chem. Phys.* **2004**, *121*, 7955−7965.
(36) Vaitheeswaran, S.; Yin, H.; Rasaiah, J. C.; Hummer, G. Water clusters in nonpolar cavities. *Proc. Natl. Acad. Sci. U.S.A.* **2004**, *101*, 17002−17005.
(37) Ross, G. A.; Bodnarchuk, M. S.; Essex, J. W. Water Sites, Networks, And Free Energies with Grand Canonical Monte Carlo. *J. Am. Chem. Soc.* **2015**, *137*, 14930−14943.
(38) Köhler, M. H.; Bordin, J. R.; de Matos, C. F.; Barbosa, M. C. Water in nanotubes: The surface effect. *Chem. Eng. Sci.* **2019**, *203*, 54−67.
(39) Striolo, A. The Mechanism of Water Diffusion in Narrow Carbon Nanotubes. *Nano Lett.* **2006**, *6*, 633−639.
(40) Cui, S. T. Molecular self-diffusion in nanoscale cylindrical pores and classical Fick's law predictions. *J. Chem. Phys.* **2005**, *123*, 054706.
(41) Seifert, G.; Joswig, J.-O. Density-functional tight binding−an approximate density-functional theory method. *Wiley Interdiscip. Rev. Comput. Mol. Sci.* **2012**, *2*, 456−465.
(42) Gaus, M.; Cui, Q.; Elstner, M. Density functional tight binding: application to organic and biological molecules. *Wiley Interdiscip. Rev. Comput. Mol. Sci.* **2014**, *4*, 49−61.
(43) Andrade-Filho, T.; Martins, T. C.; Ferreira, F. F.; Alves, W. A.; Rocha, A. R. Water-driven stabilization of diphenylalanine nanotube structures. *Theor. Chem. Acc.* **2016**, *135*, 185−188.
(44) Bystrov, V. S.; Coutinho, J.; Zelenovskiy, P. S.; Nuraeva, A. S.; Kopyl, S.; Filippov, S. V.; Zhulyabina, O. A.; Tverdislov, V. A. Molecular modeling and computational study of the chiral-dependent structures and properties of the self-assembling diphenylalanine peptide nanotubes, containing water molecules. *J. Mol. Model.* **2020**, *26*, 326−415.
(45) Beckstein, O.; Sansom, M. S. P. Liquid-vapor oscillations of water in hydrophobic nanopores. *Proc. Natl. Acad. Sci. U.S.A.* **2003**, *100*, 7063−7068.
(46) Aydin, F.; Moradzadeh, A.; Bilodeau, C. L.; Lau, E. Y.; Schwegler, E.; Aluru, N. R.; Pham, T. A. Ion Solvation and Transport in Narrow Carbon Nanotubes: Effects of Polarizability, Cation-π Interaction, and Confinement. *J. Chem. Theory Comput.* **2021**, *17*, 1596−1605.
(47) Li, Z.; Misra, R. P.; Li, Y.; Yao, Y.-C.; Zhao, S.; Zhang, Y.; Chen, Y.; Blankschtein, D.; Noy, A. Breakdown of the Nernst-Einstein relation in carbon nanotube porins. *Nat. Nanotechnol.* **2022**, *18*, 177−183.
(48) Lynch, C. I.; Rao, S.; Sansom, M. S. P. Water in Nanopores and Biological Channels: A Molecular Simulation Perspective. *Chem. Rev.* **2020**, *120*, 10298−10335.
(49) Comer, J.; Chen, R.; Poblete, H.; Vergara-Jaque, A.; Riviere, J. E. Predicting Adsorption Affinities of Small Molecules on Carbon Nanotubes Using Molecular Dynamics Simulation. *ACS Nano* **2015**, *9*, 11761−11774.
(50) Foroutan, M.; Naeini, V. F.; Ebrahimi, M. Carbon nanotubes encapsulating fullerene as water nano-channels with distinctive selectivity: Molecular dynamics simulation. *Appl. Surf. Sci.* **2019**, *489*, 198−209.
(51) Tian, C.; Kasavajhala, K.; Belfon, K. A. A.; Raguette, L.; Huang, H.; Migues, A. N.; Bickel, J.; Wang, Y.; Pincay, J.; Wu, Q.; Simmerling, C. ff19SB: Amino-Acid-Specific Protein Backbone Parameters Trained against Quantum Mechanics Energy Surfaces in Solution. *J. Chem. Theory Comput.* **2020**, *16*, 528−552.
(52) MacKerell, A. D.; Bashford, D.; Bellott, M.; Dunbrack, R. L.; Evanseck, J. D.; Field, M. J.; Fischer, S.; Gao, J.; Guo, H.; Ha, S.; et al. All-Atom Empirical Potential for Molecular Modeling and Dynamics Studies of Proteins. *J. Phys. Chem. B* **1998**, *102*, 3586−3616.
(53) Jing, Z.; Liu, C.; Cheng, S. Y.; Qi, R.; Walker, B. D.; Piquemal, J.-P.; Ren, P. Polarizable Force Fields for Biomolecular Simulations: Recent Advances and Applications. *Annu. Rev. Biophys.* **2019**, *48*, 371−394.
(54) Inakollu, V. S.; Geerke, D. P.; Rowley, C. N.; Yu, H. Polarisable force fields: what do they add in biomolecular simulations? *Curr. Opin. Struct. Biol.* **2020**, *61*, 182−190.
(55) Huang, J.; MacKerell, A. D. Force field development and simulations of intrinsically disordered proteins. *Curr. Opin. Struct. Biol.* **2018**, *48*, 40−48.
(56) Huang, J.; Simmonett, A. C.; Pickard, F. C.; MacKerell, A. D.; Brooks, B. R. Mapping the Drude polarizable force field onto a multipole and induced dipole model. *J. Chem. Phys.* **2017**, *147*, 161702.
(57) Ren, P.; Wu, C.; Ponder, J. W. Polarizable Atomic Multipole-Based Molecular Mechanics for Organic Molecules. *J. Chem. Theory Comput.* **2011**, *7*, 3143−3161.
(58) Shi, Y.; Xia, Z.; Zhang, J.; Best, R.; Wu, C.; Ponder, J. W.; Ren, P. Polarizable Atomic Multipole-Based AMOEBA Force Field for Proteins. *J. Chem. Theory Comput.* **2013**, *9*, 4046−4063.
(59) Lopes, P. E. M.; Huang, J.; Shim, J.; Luo, Y.; Li, H.; Roux, B.; MacKerell, A. D. J. Polarizable Force Field for Peptides and Proteins Based on the Classical Drude Oscillator. *J. Chem. Theory Comput.* **2013**, *9*, 5430−5449.
(60) Lin, F.-Y.; Huang, J.; Pandey, P.; Rupakheti, C.; Li, J.; Roux, B.; MacKerell, A. D. J. Further Optimization and Validation of the Classical Drude Polarizable Protein Force Field. *J. Chem. Theory Comput.* **2020**, *16*, 3221−3239.
(61) Lemkul, J. A.; Huang, J.; Roux, B.; MacKerell, A. D. An Empirical Polarizable Force Field Based on the Classical Drude Oscillator Model: Development History and Recent Applications. *Chem. Rev.* **2016**, *116*, 4983−5013.
(62) Deng, J.; Cui, Q. Electronic Polarization Is Essential for the Stabilization and Dynamics of Buried Ion Pairs in Staphylococcal Nuclease Mutants. *J. Am. Chem. Soc.* **2022**, *144*, 4594−4610.

https://doi.org/10.1021/acsomega.3c06071
ACS Omega 2023, 8, 42936−42950

(63) Jing, Z.; Liu, C.; Qi, R.; Ren, P. Many-body effect determines the selectivity for Ca^{2+} and Mg^{2+} in proteins. *Proc. Natl. Acad. Sci. U.S.A.* **2018**, *115*, E7495−E7501.
(64) Tan, Q.; Ding, Y.; Qiu, Z.; Huang, J. Binding Energy and Free Energy of Calcium Ion to Calmodulin EF-Hands with the Drude Polarizable Force Field. *ACS Phys. Chem. Au* **2022**, *2*, 143−155.
(65) Huang, J.; MacKerell, A. D. Induction of Peptide Bond Dipoles Drives Cooperative Helix Formation in the $(AAQAA)_3$ Peptide. *Biophys. J.* **2014**, *107*, 991−997.
(66) King, K. M.; Sharp, A. K.; Davidson, D. S.; Brown, A. M.; Lemkul, J. A. Impact of Electronic Polarization on Preformed, β-Strand Rich Homogenous and Heterogeneous Amyloid Oligomers. *J. Comput. Biophys. Chem.* **2022**, *21*, 449−460.
(67) Welborn, V. V.; Head-Gordon, T. Fluctuations of Electric Fields in the Active Site of the Enzyme Ketosteroid Isomerase. *J. Am. Chem. Soc.* **2019**, *141*, 12487−12492.
(68) Panel, N.; Villa, F.; Fuentes, E. J.; Simonson, T. Accurate PDZ/Peptide Binding Specificity with Additive and Polarizable Free Energy Simulations. *Biophys. J.* **2018**, *114*, 1091−1102.
(69) Pan, Z.; Huang, J.; Zhuang, W. Protein-Ligand Binding Molecular Details Revealed by Terahertz Optical Kerr Spectroscopy: A Simulation Study. *J. Australas. Ceram. Soc.* **2021**, *1*, 1788−1797.
(70) Görbitz, C. H. *CCDC 163340: Experimental Crystal Structure Determination*, 2002.
(71) The PyMOL Molecular Graphics System, Schrödinger, LLC. 2002, https://pymol.org/.
(72) Brooks, B. R.; Brooks, C. L.; Mackerell, A. D.; Nilsson, L.; Petrella, R. J.; Roux, B.; Won, Y.; Archontis, G.; Bartels, C.; Boresch, S.; et al. CHARMM: The biomolecular simulation program. *J. Comput. Chem.* **2009**, *30*, 1545−1614.
(73) Huang, J.; Rauscher, S.; Nawrocki, G.; Ran, T.; Feig, M.; De Groot, B. L.; Grubmüller, H.; MacKerell, A. D. CHARMM36m: an improved force field for folded and intrinsically disordered proteins. *Nat. Methods* **2017**, *14*, 71−73.
(74) Lin, F.-Y.; Huang, J.; Pandey, P.; Rupakheti, C.; Li, J.; Roux, B.; MacKerell, A. D. Further Optimization and Validation of the Classical Drude Polarizable Protein Force Field. *J. Chem. Theory Comput.* **2020**, *16*, 3221−3239.
(75) Jorgensen, W. L.; Chandrasekhar, J.; Madura, J. D.; Impey, R. W.; Klein, M. L. Comparison of simple potential functions for simulating liquid water. *J. Chem. Phys.* **1983**, *79*, 926−935.
(76) Lamoureux, G.; Harder, E.; Vorobyov, I. V.; Roux, B.; MacKerell, A. D. A polarizable model of water for molecular dynamics simulations of biomolecules. *Chem. Phys. Lett.* **2006**, *418*, 245−249.
(77) Darden, T.; York, D.; Pedersen, L. Particle mesh Ewald: An $N\cdot\log(N)$ method for Ewald sums in large systems. *J. Chem. Phys.* **1993**, *98*, 10089−10092.
(78) Steinbach, P. J.; Brooks, B. R. New spherical-cutoff methods for long-range forces in macromolecular simulation. *J. Comput. Chem.* **1994**, *15*, 667−683.
(79) Ryckaert, J.-P.; Ciccotti, G.; Berendsen, H. J. Numerical integration of the cartesian equations of motion of a system with constraints: molecular dynamics of n-alkanes. *J. Chem. Phys.* **1977**, *23*, 327−341.
(80) Zhang, Z.; Liu, X.; Yan, K.; Tuckerman, M. E.; Liu, J. Unified Efficient Thermostat Scheme for the Canonical Ensemble with Holonomic or Isokinetic Constraints via Molecular Dynamics. *J. Phys. Chem. A* **2019**, *123*, 6056−6079.
(81) Lamoureux, G.; Roux, B. Modeling induced polarization with classical Drude oscillators: Theory and molecular dynamics simulation algorithm. *J. Chem. Phys.* **2003**, *119*, 3025−3039.
(82) Eastman, P.; Swails, J.; Chodera, J. D.; McGibbon, R. T.; Zhao, Y.; Beauchamp, K. A.; Wang, L.-P.; Simmonett, A. C.; Harrigan, M. P.; Stern, C. D.; Wiewiora, R. P.; Brooks, B. R.; Pande, V. S. OpenMM 7: Rapid development of high performance algorithms for molecular dynamics. *PLoS Comput. Biol.* **2017**, *13*, 10056599−e1005717.
(83) Huang, J.; Lemkul, J. A.; Eastman, P. K.; MacKerell, A. D., Jr. Molecular dynamics simulations using the drude polarizable force field on GPUs with OpenMM: Implementation, validation, and benchmarks. *J. Comput. Chem.* **2018**, *39*, 1682−1689.
(84) Humphrey, W.; Dalke, A.; Schulten, K. VMD − Visual Molecular Dynamics. *J. Mol. Graph.* **1996**, *14*, 33−38.
(85) Mezei, M. Grand-canonical ensemble Monte Carlo study of dense liquid. *Mol. Phys.* **1987**, *61*, 565−582.
(86) Adams, D. Grand canonical ensemble Monte Carlo for a Lennard-Jones fluid. *Mol. Phys.* **1975**, *29*, 307−311.
(87) Ross, G. A.; Bruce Macdonald, H. E.; Cave-Ayland, C.; Cabedo Martinez, A. I.; Essex, J. W. Replica-Exchange and Standard State Binding Free Energies with Grand Canonical Monte Carlo. *J. Chem. Theory Comput.* **2017**, *13*, 6373−6381.
(88) Bodnarchuk, M.; Bradshaw, R.; Cave-Ayland, C.; Genheden, S.; Martinez, A. C.; Michel, J.; Ross, G.; Woods, C. J. P.M. S. *School of Chemistry*; University of Southampton: Southampton, U.K, 2022 (accessed March 03, 2022) www.protoms.org.
(89) Baker, E.; Hubbard, R. Hydrogen bonding in globular proteins. *Prog. Biophys. Mol. Biol.* **1984**, *44*, 97−179.
(90) Kim, J.; Han, T. H.; Kim, Y.-I.; Park, J. S.; Choi, J.; Churchill, D. G.; Kim, S. O.; Ihee, H. Role of Water in Directing Diphenylalanine Assembly into Nanotubes and Nanowires. *Adv. Mater.* **2010**, *22*, 583−587.
(91) Liu, P.; Harder, E.; Berne, B. J. On the Calculation of Diffusion Coefficients in Confined Fluids and Interfaces with an Application to the Liquid-Vapor Interface of Water. *J. Phys. Chem. B* **2004**, *108*, 6595−6602.
(92) Ding, X.; Qiu, Z.; Qu, K.; Li, Z. Molecular Dynamics Simulations of Noble Gas Fractionation during Diffusion through Silica Nanopores. *ACS Earth Space Chem.* **2019**, *3*, 62−69.
(93) Striolo, A. Water self-diffusion through narrow oxygenated carbon nanotubes. *Nanotechnology* **2007**, *18*, 475704.
(94) Thomas, M.; Corry, B.; Hilder, T. A. What Have We Learnt About the Mechanisms of Rapid Water Transport, Ion Rejection and Selectivity in Nanopores from Molecular Simulation? *Small* **2014**, *10*, 1453−1465.
(95) Huang, J.; Lopes, P. E. M.; Roux, B.; MacKerell, A. D. J. Recent Advances in Polarizable Force Fields for Macromolecules: Microsecond Simulations of Proteins Using the Classical Drude Oscillator Model. *J. Phys. Chem. Lett.* **2014**, *5*, 3144−3150.
(96) Hazel, A. J.; Walters, E. T.; Rowley, C. N.; Gumbart, J. C. Folding free energy landscapes of β-sheets with non-polarizable and polarizable CHARMM force fields. *J. Chem. Phys.* **2018**, *149*, 072317.
(97) Boulanger, E.; Thiel, W. Toward QM/MM Simulation of Enzymatic Reactions with the Drude Oscillator Polarizable Force Field. *J. Chem. Theory Comput.* **2014**, *10*, 1795−1809.
(98) Ganguly, A.; Boulanger, E.; Thiel, W. Importance of MM Polarization in QM/MM Studies of Enzymatic Reactions: Assessment of the QM/MM Drude Oscillator Model. *J. Chem. Theory Comput.* **2017**, *13*, 2954−2961.
(99) Ploetz, E. A.; Rustenburg, A. S.; Geerke, D. P.; Smith, P. E. To Polarize or Not to Polarize? Charge-on-Spring versus KBFF Models for Water and Methanol Bulk and Vapor−Liquid Interfacial Mixtures. *J. Chem. Theory Comput.* **2016**, *12*, 2373−2387.
(100) Bradshaw, R. T.; Dziedzic, J.; Skylaris, C.-K.; Essex, J. W. The Role of Electrostatics in Enzymes: Do Biomolecular Force Fields Reflect Protein Electric Fields? *J. Chem. Inf. Model.* **2020**, *60*, 3131−3144.
(101) Calvelo, M.; Lynch, C. I.; Granja, J. R.; Sansom, M. S. P.; Garcia-Fandiño, R. Effect of Water Models on Transmembrane Self-Assembled Cyclic Peptide Nanotubes. *ACS Nano* **2021**, *15*, 7053−7064.
(102) Yu, W.; Lopes, P. E. M.; Roux, B.; MacKerell, A. D.; Alexander, D. Six-site polarizable model of water based on the classical Drude oscillator. *J. Chem. Phys.* **2013**, *138*, 034508.
(103) Chen, J.; König, G. Testing and Optimizing the Drude Polarizable Force Field for Blocked Amino Acids Based on High-Level Quantum-Mechanical Energy Surfaces. *J. Comput. Biophys. Chem.* **2022**, *21*, 405−413.

https://doi.org/10.1021/acsomega.3c06071
ACS Omega 2023, 8, 42936−42950

(104) Huang, J.; Mei, Y.; König, G.; Simmonett, A. C.; Pickard, F. C.; Wu, Q.; Wang, L.-P.; MacKerell, A. D.; Brooks, B. R.; Shao, Y. An Estimation of Hybrid Quantum Mechanical Molecular Mechanical Polarization Energies for Small Molecules Using Polarizable Force-Field Approaches. *J. Chem. Theory Comput.* **2017**, *13*, 679−695.
(105) Dodin, A.; Geissler, P. L. Symmetrized Drude Oscillator Force Fields Improve Numerical Performance of Polarizable Molecular Dynamics. *J. Chem. Theory Comput.* **2023**, *19*, 2906−2917.

https://doi.org/10.1021/acsomega.3c06071
ACS Omega 2023, 8, 42936−42950